The effect of formulation morphology on stimuli-triggered co-delivery of chemotherapeutic and MRI contrast agents

Ziwei Zhang[a,b], Connor J. R. Wells[b], Gemma-Louise Davies[b,*], Gareth R. Williams[a,*]

[a] UCL School of Pharmacy, University College London, 29 – 39 Brunswick Square, London WC1N 1AX, UK

[b] UCL Department of Chemistry, University College London, 20 Gordon St, London WC1H 0AJ, UK

* Authors for correspondence. Email: gemma-louise.davies@ucl.ac.uk (GLD); g.williams@ucl.ac.uk (GRW). Tel: +44(0) 207 679 7524 (GLD); +44(0) 207 753 5868 (GRW)

Abstract

Most conventional chemotherapeutics have narrow therapeutic windows, and thus their delivery remains challenging and often raises safety and efficacy concerns. Theranostic platforms, with simultaneous encapsulation of therapeutic and diagnostic agents, have been proposed as next-generation formulations which can overcome this issue. In this work, we fabricated core@shell formulations comprising a pH responsive Eudragit L100 shell embedded with superparamagnetic iron oxide nanoparticles (SPIONs), and a thermo-responsive poly(N-isopropylacrylamide) (PNIPAM)/ethyl cellulose core loaded with the model drug carmofur. The key aim was to explore the effect of morphology (particles/fibres) on stimuli-responsive release. By varying the weight ratio of core polymer to shell polymer, the morphology of PNIPAM/ethyl cellulose@Eudragit L100 microparticles changed from concave microparticles to spherical particles. Smooth cylindrical fibres could also be generated. All the formulations exist as amorphous solid dispersions of drug-in-polymer, with distinct core@shell architectures. The fibres have clear thermo-responsive drug release profiles, while no thermo-responsive properties can be seen with the particles. All the formulations can protect SPIONs from degradation in gastric fluids (pH ~ 1.5), and around the physiological pH range the materials offer effective and pH-responsive relaxivity. The r_2 values also display clear linear relationships with drug release data, suggesting the potential of using MRI signals to track drug release *in vivo*. Mathematical equations were established to track drug release *in vitro*, with very similar experimental and predicted release profiles obtained.

1. Introduction

Advances in nanotechnology have significantly expanded the range of possible strategies for chemotherapy. Theranostic systems targeting specific sites offer the potential for major improvements in anticancer therapy, as they are capable of selectively killing tumors while also

enabling non-invasive assessment of local disease progression, quantification of carrier accumulation, and drug release (Johnson et al., 2014, Hei et al., 2017, Sokolov et al., 2017). Among a broad variety of theranostic chemical constructs and functionality, smart stimuli-responsive delivery represents one of the most commonly pursued strategies. This is because small differences in local properties between a tumor and healthy tissues can permit precise temporal and spatial delivery of therapeutic and diagnostic agents. In an effort to achieve this goal, a variety of systems have been developed responding to stimuli including temperature, ultrasound, magnetic field, light, pH, redox potential, or the presence of specific biomolecules (Chang et al., 2011, Zhao et al., 2015, Lin et al., 2017, Jha et al., 2020, Patil et al., 2020).

Thermosensitive delivery systems have been widely explored, based on the fact that body-site temperature can shift upon local infection or disease, or be changed intentionally by the application of external stimuli such as magnetic hyperthermia. Poly(N-isopropylacrylamide), PNIPAM, is the most studied thermo-responsive polymer. It exhibits typical lower critical solution temperature (LCST) behaviour: when the temperature is raised above 32 °C, a conformational change takes place from an expanded coil to a compact globule (Mano, 2008). Liu utilized PNIPAM and alginate to fabricate a thermo-sensitive hydrogel that displayed gel formation around the physiological temperature and was applied as a drug delivery vehicle for the chemotherapeutic doxorubicin (Liu et al., 2017). A dual pH and thermo-responsive gel made of carboxymethyl chitosan-graft-PNIPAM-glycidyl methacrylate was reported to give temperature-dependent release of fluorouracil (Zhang et al., 2014). The release of a hydrophilic drug incorporated inside a swollen gel can be triggered by increasing diffusion when the temperature is below the LCST, while in the case of a hydrophobic agent release can be promoted by a "squeezing" effect caused by gel collapse as the temperature is raised.

Core@shell microspheres have attracted much attention in pharmaceutical applications to enhance therapeutic efficacy and reduce the side effects of drugs (Hei et al., 2017, Hudecki et al., 2017). In terms of synthetic route, implementing consistent and reproducible methods is still challenging, and the typically low yields and time-consuming processing required also remain issues preventing such formulations from further development. Thus, facile and reproducible technologies that can produce core@shell particles are highly desirable. One such route is co-axial electrohydrodynamic atomization (EHDA). This involves the application of an electric field to a co-flowing electrically conductive fluid system to generate submicron-to-micron sized core@shell particles or fibres.

Co-axial EHDA makes it straightforward to fabricate core-shell microstructures and thus has become popular in the development of advanced carriers for multiple functional agents (Komur et al., 2017, Wen et al., 2018). For example, an acid-sensitive core-shell nanoparticle was prepared using co-axial electrospraying and subsequently linked with an antibody for the purpose of tumor-targeted, pH responsive, drug delivery. *In vitro* drug release profiles and outcomes of cytotoxicity tests showed the formulation to have targeting potential in cancer treatment (Xu et al., 2013). EHDA can easily combine a number of ingredients, including small molecules, inorganic nanoparticles or proteins, in different compartments of a formulation (Jin et al., 2016, Williams et al., 2018) Jin et al. reported a core@shell fibre system for simultaneous magnetic resonance imaging (MRI) and drug delivery in irritable bowel disease or colon cancer. Such co-delivery of therapeutic and diagnostic ingredients makes it possible to monitor disease progression during the treatment process, therefore enhancing efficacy and minimizing potential adverse effects (Jin et al., 2016).

79   While various researchers have looked at either particles or fibres, there is very little understanding
80   of how the formulation morphology affects performance of theranostics from EHDA. In this study, co-
81   axial EHDA was employed to fabricate dual-responsive MRI-based theranostic systems comprising a
82   pH responsive polymer shell loaded with superparamagnetic iron oxide nanoparticles (SPIONs), and a
83   thermo-responsive core containing the model chemotherapeutic drug carmofur. We prepared both
84   fibres and particles through a systematic variation of the processing parameters. MRI was chosen as
85   the imaging modality because of its ability to obtain high spatial and temporal resolution without the
86   risk of radiation exposure (Davies et al., 2013, Haacke and Reichenbach, 2014). To improve the
87   sensitivity and precision of diagnosis, contrast agents (CAs) are often utilized to obtain MRI images
88   with high resolution and contrast. SPIONs represent an important class of MRI CAs (Mahmoudi et al.,
89   2011), creating local magnetic field gradients to significantly decrease proton transverse relaxation
90   times (T_2) and thus boosting signal contrast (Jin et al., 2014, Neuwelt et al., 2015). Their relatively low
91   cytotoxicity and ability to be metabolized by normal biochemical pathways, alongside their magnetic
92   properties, also make SPIONs useful for a range of other biological applications, including
93   hyperthermia and magnetic targeting (Jordan et al., 1999, Laurent et al., 2011, Kang et al., 2017,
94   Perera et al., 2018).

95   Eudragit L100 was chosen to fabricate the shell. This polymer only dissolves in aqueous media with
96   pH > 6.0. To obtain good MRI contrast, SPIONs were loaded in the pH-sensitive sheath, where they
97   can be released and interact with water upon dissolution of the polymer shell. Carmofur, the
98   therapeutic agent, was confined to the core to minimise the risk of undesired premature drug release,
99   which is commonly seen in monolithic formulations. PNIPAM and ethyl cellulose, a low-cost
100   biocompatible polymer, were used to produce a thermoresponsive core compartment. Our
101   theranostic systems aimed to target co-delivery of a chemotherapeutic and MRI contrast agent to the
102   small intestine and colon. Three formulations were prepared with different ratios of core and shell
103   components and loadings of active ingredients. These were fully characterized, and their functional
104   performance assessed to elucidate the effect of morphology on potential applications.

105

106   **2.   Materials and methods**
107   2.1 Materials

108   Chemicals were purchased as follows: sodium hydroxide and anhydrous ethanol (Fisher Scientific Ltd.);
109   poly(N-isopropyl acrylamide) (average Mn 40,000), ethyl cellulose (48% ethoxyl, viscosity 10 cP, 5 %
110   in toluene/ethanol 80:20(lit.)), sodium chloride, N,N-dimethylacetamide (DMAc), dimethylformamide,
111   acetone, anhydrous ethanol, polyvinylpyrrolidone (PVP; 40 kDa), hydroxylamine hydrochloride, o-
112   phenanthroline, xanthan gum, $FeCl_3 \cdot 6H_2O$ and $FeCl_2 \cdot 4H_2O$ (Sigma-Aldrich); Eudragit L100 (MW 12,500,
113   Röhm GmbH); and, carmofur (ChemCruz™). Ultrapure water was collected from a Millipore MilliQ
114   system operated at 18.2 MΩ.

115   2.2 Synthesis of SPIONs

116   $FeCl_3 \cdot 6H_2O$ (6.5 g, 0.024 mol) and $FeCl_2 \cdot 4H_2O$ (2.48 g, 0.012 mol) were dissolved in 25 mL of
117   deoxygenated ultrapure water. This solution was added dropwise into 250 mL of an aqueous NaOH
118   solution (0.5 M) at 40 °C, and stirred for 1 h at this temperature. The resultant SPIONs were washed
119   by centrifugation with DI water until the supernatant was pH neutral, and the resultant black
120   precipitate dried under vacuum. For PVP stabilisation, SPIONs (100 mL, 10 mg/mL in water) were

121 mixed with 2 mL of an aqueous PVP solution (25.6 g/L, 0.64 mM), and the suspension was shaken (100
122 rpm) at room temperature. After 24 h, the suspension was mixed with 500 mL of aqueous acetone
123 (H_2O/acetone, 1:10 v/v) and centrifuged at 13,200 rpm for 20 min. The supernatant was removed, and
124 the resultant black precipitate washed with ethanol and dried in an oven at 50 °C for 24 h.

125 2.3 Measurement of lower critical solution temperature (LCST)

126 The LCST of PNIPAM was determined using a UV−Vis spectrophotometer (Cary 60 instrument, Agilent)
127 with 1 wt% aqueous polymer solutions, by measuring absorption at 670 nm over the temperature
128 range of 20−60 °C. The experiments were carried out with 3 heating/cooling cycle using a water bath
129 (temperature ramp of 2 °C/min) and the transmittance was recorded every 5 seconds. The LCST was
130 identified as the temperature at which the absorption of the sample was 50% of the maximum value.

131 2.4 Preparation of working fluids and EHDA

132 After a series of preliminary optimization experiments, co-axial EHDA was used to produce core@shell
133 microparticles comprising a Eudragit L100 shell loaded with SPIONs and a PNIPAM/ethyl cellulose core
134 (PNIPAM/EC) loaded with carmofur. The recipes are shown in Table 1. Eudragit L100 was dissolved in
135 a mixture of DMAc and ethanol (2:8 v/v). PNIPAM and ethyl cellulose were dissolved in a solvent
136 system comprising DMF and ethanol (3:7 v/v). Single fluid processing was employed to produce
137 PNIPAM/ethyl cellulose particles or Eudragit L100 fibres loaded with SPIONs and carmofur as controls.
138 For PNIPAM/EC particles, a solution of 4% (w/v) ethyl cellulose and 4% (w/v) PNIPAM was prepared in
139 a mixture of DMF and ethanol (3:7 v/v). For Eudragit L100 fibres and microparticles, a 12 % (w/v) or
140 4 % (w/v) solution of Eudragit L100 was prepared in a mixture of DMAc and ethanol (2:8 v/v). Polymer
141 solutions were stirred vigorously for 24 h, then carmofur (to give final concentrations of 4, 8 or 12
142 mg/mL) and PVP-SPIONs (at final concentrations of 4, 8 or 12 mg/mL) were added to the solutions of
143 PNIPAM/ethyl cellulose or Eudragit L100 with sonication for 20 min.

144

145

146 Table 1

147 Formulations of core@shell microparticles and fibres loaded with carmofur and SPIONs.

ID	Core		Sheath		EC : PNIPAM : Eudragit L100 : Carmofur : PVP-SPIONs weight ratio [d]
	Polymer (w/v) [a]	Carmofur (w/w) [b]	Polymer (w/v) [a]	PVP-SPIONs (w/w) [c]	
P-EC@EL-M1	2.5 % EC		4 %		61 : 11 : 11 : 5 : 12
	2.5 % PNIPAM	23.33 %	Eudragit L100	20 %	
P-EC@EL-M2	4 % EC		4 %		53 : 15 : 15 : 6 : 11
	4 % PNIPAM	20 %	Eudragit L100	20 %	
P-EC@EL-M3	6 % EC		4 %		45 : 19 : 19 : 7 : 10
	6 % PNIPAM	18 %	Eudragit L100	22.5 %	
P-EC@EL-F	8 % EC		12%		61 : 12 : 12 : 4 : 11
	8 % PNIPAM	18 %	Eudragit L100	18 %	

148 *(a: % w/v ratio of polymer to solvent; b: % w/w ratio of carmofur to core polymer; c: % w/w ratio of PVP-*
149 *SPIONs to shell polymer; d: weight ratio of the different components in the final formulations)*

150 An HCP 35-35000 power supply (FuG Elektronik GmbH) was employed to provide an electric field. For
151 single fluid EHDA, the spinning solution was loaded into a 5 mL syringe fitted with a stainless-steel
152 needle (18G). Great care was taken to avoid air bubbles in the solution. An alligator clip (the positive
153 electrode) was then attached to the concentric needle. The grounded electrode was connected to an
154 aluminium plate. EHDA was performed under ambient conditions (22 ± 3 °C and relative humidity 40
155 ± 5%). A syringe pump (KDS 100, Cole-Parmer) was used to drive the working solutions. To produce
156 PNIPAM-EC particles, the working voltage was fixed at 18 kV, with a collector distance of 20 cm and a
157 flow rate of 0.8 mL/h. To produce Eudragit L100 formulations, the working voltage was fixed at 16 kV,
158 with a collector distance of 15 cm from the needle and a flow rate of 0.8 mL/h.

159 For co-axial EHDA, two syringe pumps (KDS 100, Cole Parmer) were employed to control the sheath
160 (0.7 mL/h) and the core (0.2 mL/h) flow rates. The voltage was fixed at 14 kV, with the collector placed
161 20 cm from the needle. A concentric spinneret was employed (core needle: 27G; outer and inner
162 diameters of 0.42 and 0.21 mm, respectively; shell needle: 18G; outer and inner diameters of 1.25 and
163 0.84 mm).

164 2.5 Characterization

165 A MiniFlex 600 diffractometer (Rigaku) supplied with Cu-Kα radiation was used to collect XRD patterns
166 (λ = 0.15418 nm, 40 kV, 15 mA). Patterns were recorded over the 2θ range from 5 to 70° (step = 0.01°).
167 The morphology of the formulations was analysed by a field emission scanning electron microscope
168 (FEI Quanta 200F) connected to a secondary electron detector (Everheart-Thornley Detector). Samples

were coated with a 20 nm gold sputter (using a Quorum Q150T coater) before measurement. The size distribution of the formulations was determined from the SEM micrographs by measuring at > 100 points in the images, with the aid of the ImageJ software (version 1.52s, National Institutes of Health).

Transmission electron microscopy images of specimens were obtained on a JEOL JEM-1200 microscope operated at 120 kV with a beam current of ca. 80 mA. A Gatan Orius 11-megapixel camera was used to take images. Average particle size was measured with the ImageJ software (version 1.52s, National Institutes of Health).

Thermogravimetric analysis was undertaken on a Discovery instrument (TA Instruments, Waters LLC). Ca. 3 mg of each sample was loaded into an aluminium pan and heated from 40 to 500 °C at 10 °C/min under a nitrogen flow of 25 mL/min. Data were recorded using the Trios software and analysed with TA Universal Analysis. A Q2000 instrument (TA Instruments, Waters LLC) was used for DSC measurements. A small amount of sample (approximately 3 mg) was loaded in a non-hermetically sealed aluminium pan (T130425, TA instruments) and experiments carried out with a temperature ramp of 10 °C/min and nitrogen purge of 25 mL/min. DSC data were recorded with the TA Advantage software package and analysed using TA Universal Analysis.

2.6 Stability assay

Stability studies were carried out by dispersing 10 mg of the formulations or 2 mg of PVP-SPIONs in 25 mL of an aqueous HCl solution (pH 1.5). Experiments were carried out in a shaking incubator (100 rpm) at 37 °C for 2 h. The resulting solutions were centrifuged for 15 min (13,200 rpm) to sediment any undissolved particles. 5 mL samples of the supernatants were removed and neutralized with a few drops of aqueous 0.2 M NaOH. 0.9 mL of the neutralized sample was added to 0.3 mL of a 10 % (w/v) hydroxylamine hydrochloride solution in water and 0.6 mL of an aqueous 0.2 % (w/v) o-phenanthroline solution.

2.7 Loading capacity and encapsulation efficiency

To calculate the loading capacity (LC) and encapsulation efficiency (EE) of carmofur, 10 mg of the formulations was added into 10 mL of ethanol and sonicated until the polymer was fully dissolved. A PVDF-type syringe filter (0.22 μm) was used to filter the resultant solutions, and the filtrates centrifuged for 10 min (13,200 rpm) to remove the SPIONs. The supernatants were analyzed with UV spectroscopy at 262 nm (Cary 100 instrument, Agilent), and the LC and EE calculated based on a pre-determined calibration curve.

2.8 *In vitro* drug release

To mimic the conditions encountered in oral administration, drug release experiments were first performed in an acidic solution (pH 1.5, HCl) to simulate the gastric fluid (37 °C) for 1 hour, and then in a PBS buffer (pH 7.4) or acetate buffer (pH 5.5) at 37 °C or 25 °C. 20 mg samples and 10 mL of pre-heated pH 1.5 media were added into dialysis bags (MWCO 3500) and transferred to 30 mL of the same buffer at 37 °C. After a 1 h incubation, some of dialysis bags were removed and the acidic media replaced with 10 mL of fresh PBS buffer (pH 7.4) or acetate buffer (pH 5.5) at 37 or 25 °C. The refreshed samples in dialysis bags were transferred to 30 mL of the relevant buffer at the appropriate temperature. Experiments were undertaken in a shaking incubator (100 rpm). 1 mL aliquots were withdrawn from the dissolution medium at predetermined time points and filtered through a PVDF-type syringe filter (0.22 μm). To maintain a constant volume, 1 mL of fresh pre-heated buffer was

210 added to the dissolution vessel. In the temperature-triggered release experiments, samples (n=6)
211 were immersed in 5 mL of pre-heated acetate buffer (pH 5.5, 37 °C) and transferred into a dialysis bag
212 (MW 3500), which was in turn submerged into 20 mL of the same buffer (pH 5.5) and incubated at
213 37 °C (100 rpm). After a 45 min incubation, half the samples (n=3) were transferred to the same buffer
214 pre-heated at 25 °C (100 rpm). 0.5 mL aliquots were periodically withdrawn from the dissolution
215 medium and filtered through a PVDF-type syringe filter (0.22 μm). To maintain a constant volume, 0.5
216 mL of fresh pre-heated buffer was added to the dissolution vessel.

217 In all cases, the filtrates were centrifuged for 15 min (13,200 rpm) to remove any SPIONs, and then
218 analysed with an Agilent Cary 100 spectrophotometer. Carmofur quantification was performed at λ_{max}
219 of 262 nm. Dilutions were undertaken where necessary to bring concentrations into the linear range
220 of the calibration curve. Experiments were performed in triplicate and the results are reported as
221 mean ± standard deviation (S.D.).

222 2.9 Proton relaxivity

223 First, the SPION contents in the samples were determined. Samples (containing ca. 0.06 mg SPIONs)
224 were digested using hot HNO3 digestion and then diluted to 10 mL with deionized water. The iron
225 concentrations (mM) were quantified on a Varian 720-ES inductively coupled plasma atomic emission
226 spectroscopy (ICP-AES). The samples were measured against a standard containing Fe ions (100 mg·L^{-}
227 ^{1} in 5% HNO3).

228 An MQC+ benchtop NMR analyser (Oxford Instruments) was used to measure the transverse
229 relaxation times (T_2) of protons at 37 °C and 23 MHz. The Carr-Purcell-Meiboom-Gill (CPMG) method
230 was used to measure T_2, with 4 scans per experiment. The water relaxation rate enhancement per
231 mmol of contrast agent (relaxivity) is defined by Equation 1.

232 $$r_2 = \frac{R_{2,obs} - R_{2,sol}}{[CA]} \qquad (1)$$

233 Where r_2 is the relaxivity, $R_{2,obs}$ is the observed transverse relaxation rate of the agent in aqueous
234 suspension ($R_2 = 1/T_2$), $R_{2,sol}$ is the relaxation rate of the unaltered solvent system (*i.e.* in the absence
235 of contrast agent) and [CA] is the mM concentration of the contrast agent in suspension, as measured
236 by ICP-MS.

237 To monitor changes in proton relaxivity with pH and temperature, a dispersion of approximately 16
238 mg of each formulation in 8 mL of a 0.1 % (w/v) aqueous xanthan gum solution was placed into a 10
239 mm-diameter NMR tube, which was held at 37 °C. The transverse relaxation time (T_2) was directly
240 monitored over 24 h. At predetermined time points, 0.3 mL of suspension was taken from the NMR
241 tube, diluted, and filtered through a PVDF-type syringe filter (0.22 μm). To measure the free iron
242 concentration, suspensions were analysed by ICP-MS after hot nitric acid digestion. To measure the
243 carmofur concentration, centrifugation (13,200 rpm for 10 min) was conducted to remove the SPIONs,
244 and the supernatant analysed on an Agilent Cary 100 spectrophotometer. All experiments were
245 performed in triplicate and the results are reported as mean ± S.D. In a set of experiments to predict
246 drug release, dispersions of fibre samples (1.0 mg/mL) in 0.1% w/v xanthan gum at pH 7.4 (n=3) were
247 placed into 10 mm NMR tubes. At selected time points, 0.3 mL aliquots were taken from the NMR
248 tube and the carmofur content in each aliquot quantified as above.

249

3. Results

3.1 Physicochemical and structural properties

Polyvinyl pyrrolidone (PVP) stabilized superparamagnetic iron oxide nanoparticles (PVP-SPIONs) were synthesized using the method described in our previous study (Zhang et al., 2020). The PVP-SPIONs possessed a mean size of 8.5 ± 2.7 nm, as determined by transmission electron microscopy (TEM; Supplementary Information, Fig. S1A). X-ray diffraction (XRD) confirms the synthesis of SPIONs (Fig. S1B). The reflections at 30.2, 35.5, 43.7, 53.6, 57.1 and 62.9° can be indexed to the (022), (311), (004), (333), (115), and (044) planes of the cubic inverse spinel Fe_3O_4 (ICSD entry 77592).

The LCST of PNIPAM were determined by measuring the turbidity changes of the polymer solution with temperature. The LCST is defined here as the temperature corresponding to 50% of the maximum transmittance at 670 nm (with a polymer concentration of 1 wt%). Fig. S1C shows PNIPAM has an LCST of 35.7 °C. The polymer is found to be able to transition through the LCST reversibly, without any shift in the cloud point being seen after three cycles of cooling and heating. Hysteresis can be observed in all the heat/cool curves; this is seen because a water bath was used to control the temperature ramp (2 °C/min), leading to a slight delay in temperature changes of the polymer solutions, and thus hysteresis in the PNIPAM conformational changes.

A mixed solution of PNIPAM and ethyl cellulose (EC) can be independently electrosprayed. Prior to preparing core@shell microparticles, the electrospraying parameters were optimized for a core polymer blend loaded with 10 wt% SPIONs and 10 wt% carmofur. The resultant PNIPAM-EC particles had a broad size distribution and rough surfaces, with mean particle diameters of 0.75 ± 0.50 μm as measured by ImageJ (Fig. S2). The processing parameters for the shell polymer, Eudragit L100 were also optimized. Monolithic Eudragit L100 fibres and microparticles loaded with 10 wt% PVP-SPIONs and 10 wt% carmofur were obtained (Fig. S3), with mean fibre diameter of 0.61 ± 0.16 μm and particle size of 0.38 ± 0.22 μm, respectively.
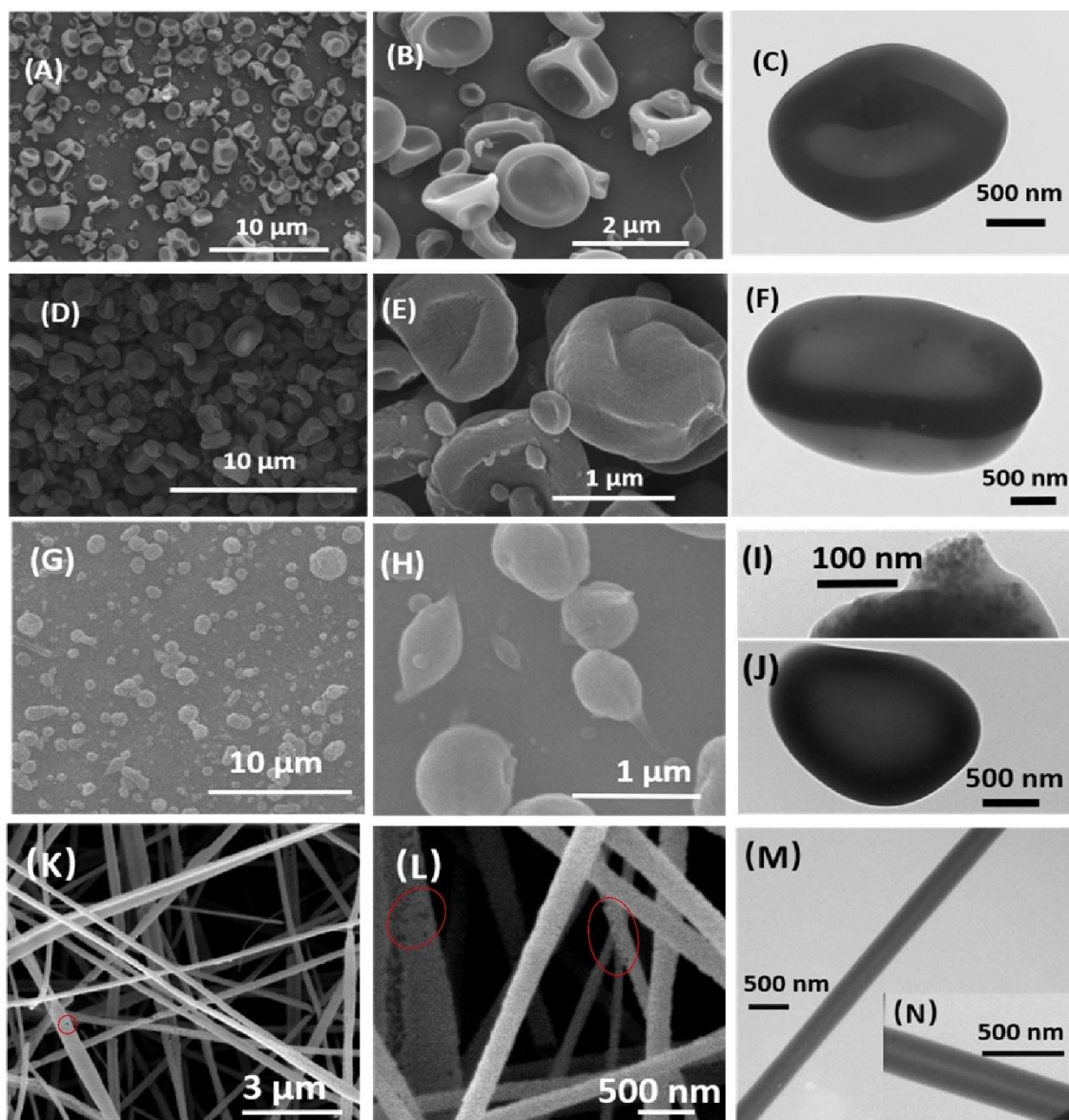
Fig. 1. SEM and TEM images for P-EC@EL-M1 (A, B, C); P-EC@EL-M2 (D, E, F); P-EC@EL-M3 (G, H, I, J); and, P-EC@EL-F (K, L, M, N).

Three microparticle and one fibre formulations were produced with a range of core@shell compositions, as shown in Table 1. SEM and TEM images of P-EC@EL-M1, 2, 3 and P-EC@EL-F are shown in Fig. 1. The core@shell microparticles have distinct morphology from the PNIPAM-EC material. SEM images of P-EC@EL-M1 (Fig. 1A,B) display a concave shape with smooth surface, and a mean size of 0.98 ± 0.40 µm (Fig. S4). P-EC@EL-M2 comprises concave particles, but these are more spherical in shape due to the larger w/w ratio of core polymer to shell polymer, and have sizes of 1.05 ± 0.44 µm (Fig. 1D,E, Fig. S4). The SEM images of P-EC@EL-M3 depict roughly spherical particles with a diameter of 1.00 ± 0.41 µm (Fig. 1G,H, Fig. S4). It is clear that the morphology of the microparticles is related to the core to shell polymer w/w ratio, with an increasing proportion of core polymer leading to more spherical particles. TEM images (Fig. 1C, F, I, J) showed that all three particles have two compartments. For P-EC@EL-M3, a clear dark halo can be found, consistent with a shell compartment containing PVP-

289 SPIONs. The two compartments in P-EC@EL-M1 and 2 are overlaid, which might be due to the concave
290 shape of the particles. The shell compartment is darker, indicating the encapsulation of SPIONs, while
291 the core loaded with carmofur is lighter. For P-EC@EL-F, SEM images (Fig. 1K, L) reveal linear cylindrical
292 structures with mean diameters of 0.42 ± 0.13 μm (Fig. S4). A small number of pores were present on
293 the fibre surface (marked in red circles, Fig. 1K, L), which might because of the slower evaporation rate
294 of the core solvent. No 'beads-on-a-string' morphology was observed and no evidence for any particles
295 or phase separation was present, which indicates the components of the fibres are homogeneously
296 mixed. P-EC@EL-F also has a clear core@shell structure (Fig. 1M, N). P-EC@EL-M1, 3 and P-EC@EL-F
297 were selected for further study, since they have very distinct morphologies.
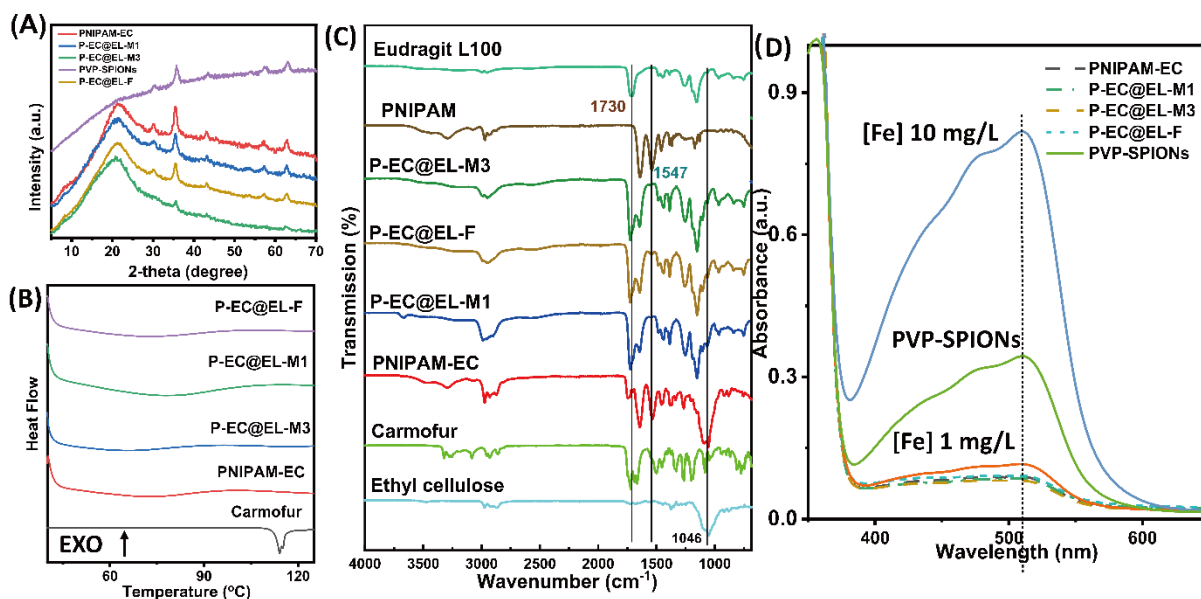
298

299 Fig. 2. Physicochemical characterisation of the materials. (A) XRD patterns of PNIPAM-EC, P-EC@EL-
300 M1, M3, P-EC@EL-F and PVP-SPIONs. (B) DSC profiles and (C) FTIR spectra of PNIPAM-EC, P-EC@EL-
301 M1, M3, P-EC@EL-F and carmofur. (D) The results of colorimetric assays to determine [Fe] in solution
302 for PVP-SPIONs, P-EC@EL-M1, P-EC@EL-M3 and P-EC@EL-F after immersion in pH 1.5 aqueous HCl
303 for 2 h, with two control FeCl₃ aqueous solutions (blue and orange, 1 and 10 mg/L respectively).

304

305 The XRD patterns of the formulations are displayed in Fig. 2A. The characteristic reflections of cubic
306 inverse spinel Fe_3O_4 can be observed in P-EC@EL-M1, M3 and P-EC@EL-F, indicating successful loading
307 of PVP-SPIONs into the formulations. The broad peak between 10-30° arises due to the amorphous
308 nature of the polymers after processing by EHDA. The characteristic reflections of carmofur and EC
309 (Fig. S5A) are not observed in the XRD patterns of any of the formulations, demonstrating that they
310 are present in the amorphous form owing to the very rapid drying which occurs during EHDA. This is
311 supported by DSC analysis (Fig. 2B and Fig. S5B). Pure carmofur clearly exists as a crystalline material
312 with two sharp endothermic melting peaks visible at ca. 114 and 115 °C, consistent with the literature
313 (Sanchez-Vazquez et al., 2017). The raw Eudragit, EC and PNIPAM polymers have a broad endothermic
314 peak between 60 to 120 °C, attributed to the loss of adsorbed water and solvent (ethanol, DMF). No
315 events can be observed in the DSC profile for PVP-SPIONs. The absence of the carmofur melting
316 endotherm in the DSC curves of the drug loaded microparticles confirms that it is present in the form
317 of an amorphous solid dispersion, which is consistent with our previous study (Zhang et al., 2020).

Fig. 2C displays the FTIR spectra of PNIPAM-EC, P-E@EL-M1, M3 and P-E@EL-F, together with the raw materials. Carmofur displays typical absorption bands at 1666-1720 cm^{-1} and at 1495 cm^{-1}, related to C=O stretching vibrations. As a co-polymer of methacrylic acid and methyl methacrylate, Eudragit L100 has a characteristic stretch at 1730 cm^{-1} that arises from C=O vibrations of ester groups. For EC, a strong band at 1046 cm^{-1} can be attributed to C-O stretching, while the vibration at 1547 cm^{-1} in the PNIPAM spectra is the amide N-H bending. For the PNIPAM-EC microparticles, the characteristic stretches of ethyl cellulose, carmofur and PNIPAM can be clearly identified in the spectra. With the core@shell formulations, characteristic stretches of Eudragit L100, ethyl cellulose and PNIPAM also can be seen. The C=O stretching vibrations around 1730 cm^{-1} become more intense in the composites, as they incorporate the stretches of carmofur between 1666-1720 cm^{-1}. This suggests the successful incorporation of carmofur in the formulations.

TGA and DTA profiles (Fig. S6) confirmed the existence of both carmofur and PVP-SPIONs within the composite formulations. P-EC@EL-M1, M3 and P-EC@EL-F display multistage decomposition processes. The small mass loss of about 3 % before 100 °C can be attributed to solvent loss (e.g. ethanol, DMF, physiosorbed water). Two processes at around 120 and 240 °C can be attributed to the decomposition of carmofur, and the mass loss beyond 300 °C is associated with polymer matrix degradation. From the TGA results of the microspheres, we can calculate that the iron oxide content is 12.1 % w/w for P-EC@EL-M1, 10.4 % w/w for P-EC@EL-M1, and 10.3 % w/w for P-EC@EL-F. This corresponds to an encapsulation efficiency (EE) of ca. 100%, consistent with the theoretical SPION loading amount (12, 10, 10 % w/w, respectively). The carmofur loadings of P-EC@EL-M1, P-EC@EL-M3 and P-EC@EL-F were calculated by UV-vis spectroscopy, and found to be 4.9 ± 0.3 %, 7.1 ± 0.8 % and 5.1 ± 0.4 % w/w respectively, with EEs of 96.6 ± 6.0 %, 93.5 ± 11 and 94.8 ± 7.0 % (mean ± S.D., n = 3).

3.2 Stimuli responsive properties

Bare SPIONs are unstable in highly acidic environments such as those found in the stomach, resulting in their oxidation and eventual degradation. Their encapsulation in Eudragit L100-coated formulations is expected to resolve this issue, with the protective sheath preventing degradation in gastric fluids (Rose et al., 2016). To test the stability of encapsulated SPIONs, 10 mg of our formulations were incubated in 25 mL of pH 1.5 aqueous HCl solution, similar to the pH of gastric liquids (Evans et al., 1988). 2 mg of PVP-SPIONs was treated under the same conditions. The Fe concentration freed into solution was measured using an *o*-phenanthroline colorimetric assay after incubation at 37 °C for 2 h, mimicking the gastric transit time, and subsequent neutralisation. The λ_{max} of the ferrous tris-*o*-phenanthroline product of dissolved iron and *o*-phenanthroline is around 512 nm at neutral pH. Fig. 2D shows that the [Fe] released from the core@shell materials was below that of a control FeCl$_3$ aqueous solution ([Fe] 1 mg/L, orange line), indicating less than 2.5 wt.% of the total SPION content was degraded in the loaded fibres This concentration is significantly lower than the [Fe] released from bare PVP-SPIONs at equivalent concentrations (between 1-10 mg/L, equating to up to 12.5 wt.% degradation, green line). These results show that the Eudragit L100 coating can protect the SPIONs from degradation in an acidic environment. SEM images (Fig. S7) of the formulations following acid incubation confirm the stability of the formulations: as a result of matrix swelling, P-EC@EL-M1 become more spherical, while hollow structures still can be observed for the P-EC@EL-M3 microparticles. The morphology of P-EC@EL-F appears largely unaffected after exposure to the acidic conditions.

To mimic the conditions encountered during oral delivery, drug release experiments were carried out at different pHs. Initially, samples were incubated at pH 1.5 (aqueous HCl solution, mimicking the gastric pH) for 1 h at 37 °C, and then subsequently transferred to pH 7.4 or 5.5 buffer at 37 or 25 °C (representing the pH of the intestinal tract and the tumor microenvironment, respectively). 25 °C (a temperature below the LCST of PNIPAM) was used as the second test temperature to explore the dissolution profile of our formualtions in intesntial tract. Although 25 °C is lower than the physiological temperature, these experiments offer a good insight into the temperature-responsive behavior of the formulation matrix and how it might affect the drug release. Furthermore, low temperature treatment such as cryotherapy has been used in ablation of colorectal and intestinal tumor (Primrose 2002, Parsi, Trindade et al. 2017), and thus there is a possibility to utilize hypothermia to manipulate drug release in the intestinal tract.

The results of *in vitro* dissolution tests are given in Fig. 3. In the first hour, as a result of Eudragit L100 being insoluble in acidic conditions and the drug embedded in the core, there is relatively little carmofur release. Only 20 % of the drug in P-EC@EL-F was released into the dissolution medium, much reduced compared to the monolithic Eudragit L100 fibres (35 %, Fig. S8A). However, over 40% of carmofur was freed from PNIPAM-EC, P-EC@EL-M1 and M3 into the acidic environments. The rapid release from the core@shell particles might be due to the particle structure. Though the core@shell microparticles seem to possess clear edges between the two compartments in TEM images, some of the core and shell solutions may have mixed during EHDA processing leading to carmofur being present at the particle surface. This drug on the surface will be freed quickly into solution and generate pores on the particle surface. This effect is magnified since the core@shell particles have very high surface area to volume ratios as a result of their small size. Once pores are created, drug from further inside the particles can easily diffuse out. Pores through which drug molecules could escape from the microparticles could also be created by swelling of the L100 shell and the permeation of water into the particle centre.

When the microparticles were transferred into a neutral PBS or pH 5.5 acetate medium there was very rapid release noted, with 80 % cumulative release reached in 3 hours (see Fig. 3A-C). This is observed at both 25 and 37 °C, with only slightly reduced rates observed at the lower temperature. Release is also marginally slower at pH 5.5 than 7.4, but again this trend is not particularly marked. The particle formulations thus have only minimal ability to discriminate between different conditions of temperature and pH. To test this hypothesis, an experiment was performed where particles or fibres were immersed in a pH 1.5 solution for 24 h (Fig. S8B). Here, all three microparticles gave more than 80 % release of carmofur with a plateau reached after 5 h, confirming their lack of pH-responsive properties.

For P-EC@EL-F (Fig. 3D), a burst release can be seen in the first 4 h after transfer from the pH 1.5 buffer to PBS, reaching > 80 % cumulative release, while in HCl only around 50% of the drug were released over 4 h (Fig. S8B). Release at 37 °C is notably lower than at 25 °C. At pH 5.5 (Fig. 3E), the fibres display slower release and a distinctly thermo-responsive release profile. Faster release rates and higher cumulative release percentages are found at 25 °C. The difference in release profile at the two pHs can be attributed to the solubility of the Eudragit L100 shell, which can reduce the release of carmofur at pH 5.5 and triggers rapid release when in pH 7.4 PBS.

In contrast to the microparticles therefore, the core@shell fibres display thermo-responsive properties. This difference in behaviour is thought to be because of the difference in structures. The

microparticles have smaller sizes and are more easily dispersed in buffers, allowing water to effectively get access to their core via swelling of the Eudragit L100 shell. The higher surface area to volume ratios of the particles can further facilitate interactions between water and the formulations, resulting in rapid carmofur release. In contrast, the Eudragit L100 shell of the fibres can minimize release at pH 1.5, but triggers rapid release at neutral pH. This is promising for the treatment of intestinal diseases via oral administration.
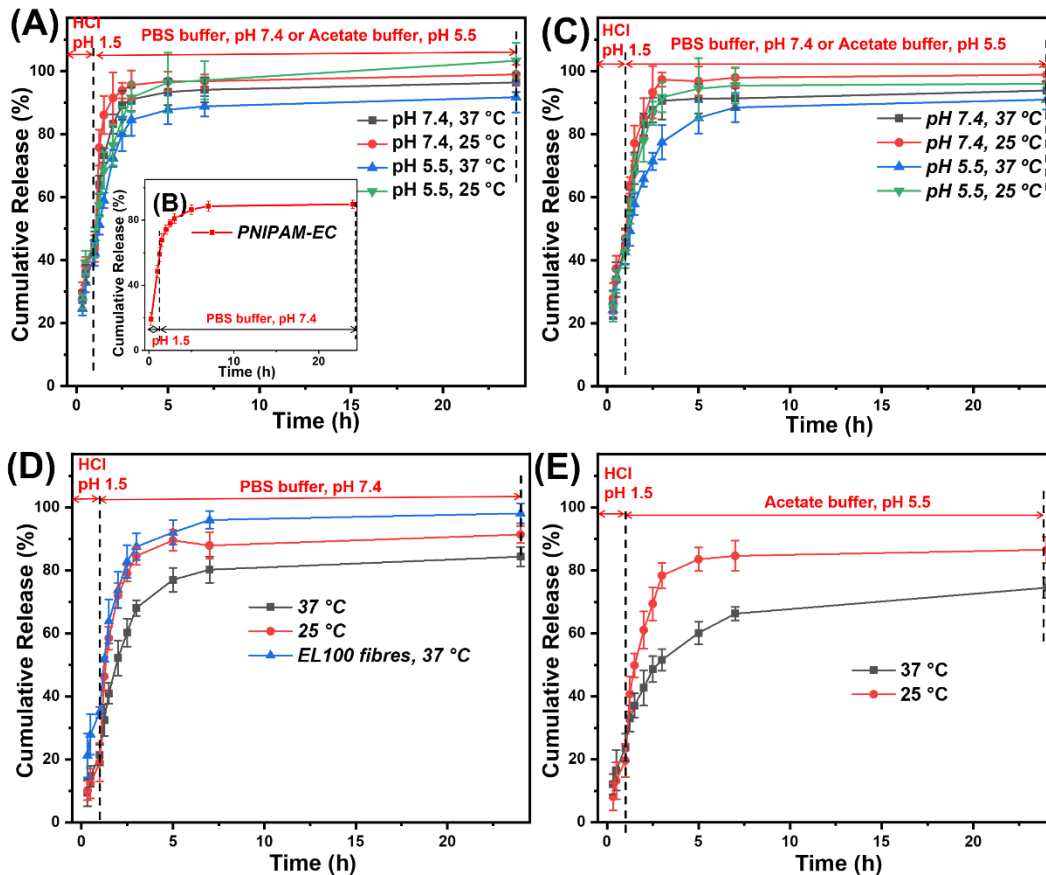
Fig. 3. Plots showing the release of carmofur from (A) P-EC@EL-M1, (B) PNIPAM-EC, (C) P-EC@EL-M3 and (D and E) P-EC@EL-F, as measured by UV-vis spectroscopy. Data are given from three independent experiments as mean ± S.D.

Further experiments were performed to investigate the thermo-responsiveness of the P-EC formulations, as shown in Fig. S9. Samples (n=6) were firstly incubated at pH 5.5 and 37 °C for 45 min, and then half of these samples were transferred to a 25 °C water bath (stirred at 50 rpm). Carmofur release was monitored by UV-vis measurement of the supernatant at selected time points. The results further confirm the thermo-responsive release profile of P-EC@EL-F. Compared to the release curves at 37 °C, with approx. 62 % release over 180 min, faster release was observed when the formulations were transferred to 25 °C conditions, where over 80 % of the total drug content was released. Much reduced differences were observed with the core@shell microparticles.

SPIONs are typically T_2 contrast agents, providing negative contrast by decreasing the transverse relaxation time of local protons. To explore the efficiency of their contrast behaviour when encapsulated within the composite formulations, the relaxivity (r_2) was calculated according to

425   Equation 1. In a previous study, we fabricated monolithic Eudragit fibres loaded with SPIONs and
426   carmofur and monitored the r_2 relaxivity as a function of time. The resultant r_2 relaxivity could be
427   correlated with the extent of drug and SPIONs release (Zhang et al., 2020). In this work, SPIONs and
428   carmofur were separately embedded into the pH-sensitive Eudragit L100 shell and thermoresponsive
429   core. The r_2 relaxivity was monitored as a function of time during incubation in different pH buffers
430   with 0.1 % w/v xanthan gum (pH 5.5, 6.5 or 7.4) at 37 or 25 °C. The resultant r_2 relaxivity profiles were
431   evaluated to determine whether the changing MRI signal with SPION release could be employed to
432   track coincident carmofur release.

433   Firstly, the relaxivity of the PNIPAM-EC microparticles was explored. A very low (less than 4 mM^{-1}·s^{-1})
434   increase in relaxivity over 24 h was observed at both temperatures (Fig. S10), with r_2 increasing from
435   0.30 ± 0.1 mM^{-1}·s^{-1} at 10 min to 2.5 ± 1.5 mM·s^{-1} after 24 hours at 25 °C. The low relaxivity is thought
436   to be due to many of the SPIONs being encapsulated into insoluble EC regions of the matrix, preventing
437   their effective magnetic interactions with diffusive water protons (Angelakeris, 2017).

438   Fig. 4A-C displays the r_2 relaxivity profiles of the core@shell materials as a function of incubation time.
439   Due to the very low initial relaxivity values, profiles were monitored from 10 min immersion onwards.
440   The recovery of r_2 can be regarded as a kinetic process which is proportional to the dissolution of the
441   ES100 shell layer (Zhang et al., 2020). For P-EC@EL-M1, it can be seen that the transverse relaxivity
442   gradually increases over 24 hours at pH 7.4. At all timepoints studied and both temperatures, relaxivity
443   at pH 7.4 is higher than at pH 6.5. The pH-responsive relaxation profile is analogous to previous results,
444   and expected to arise from the release and potential micellisation of SPIONs during the dissolution of
445   Eudragit L100. At pH 5.5, the relaxivity remains low over 24 hours (less than 2.2 mM^{-1}·s^{-1}) because the
446   Eudragit L100 is insoluble. While some drug release can occur via carmofur in the core reaching the
447   dissolution medium through diffusion or swelling of the polymer and the permeation of water into
448   the centre of the polymer matrix, the larger SPIONs cannot exit the formulations via the same route.
449   The relaxation behaviors of P-EC@EL-M3 and P-EC@EL-F are similar to that of P-EC@EL-M1. As shown
450   in Fig. 4D-F, the transverse relaxivity of all three formulations is largely influenced by pH, but much
451   less so by temperature.
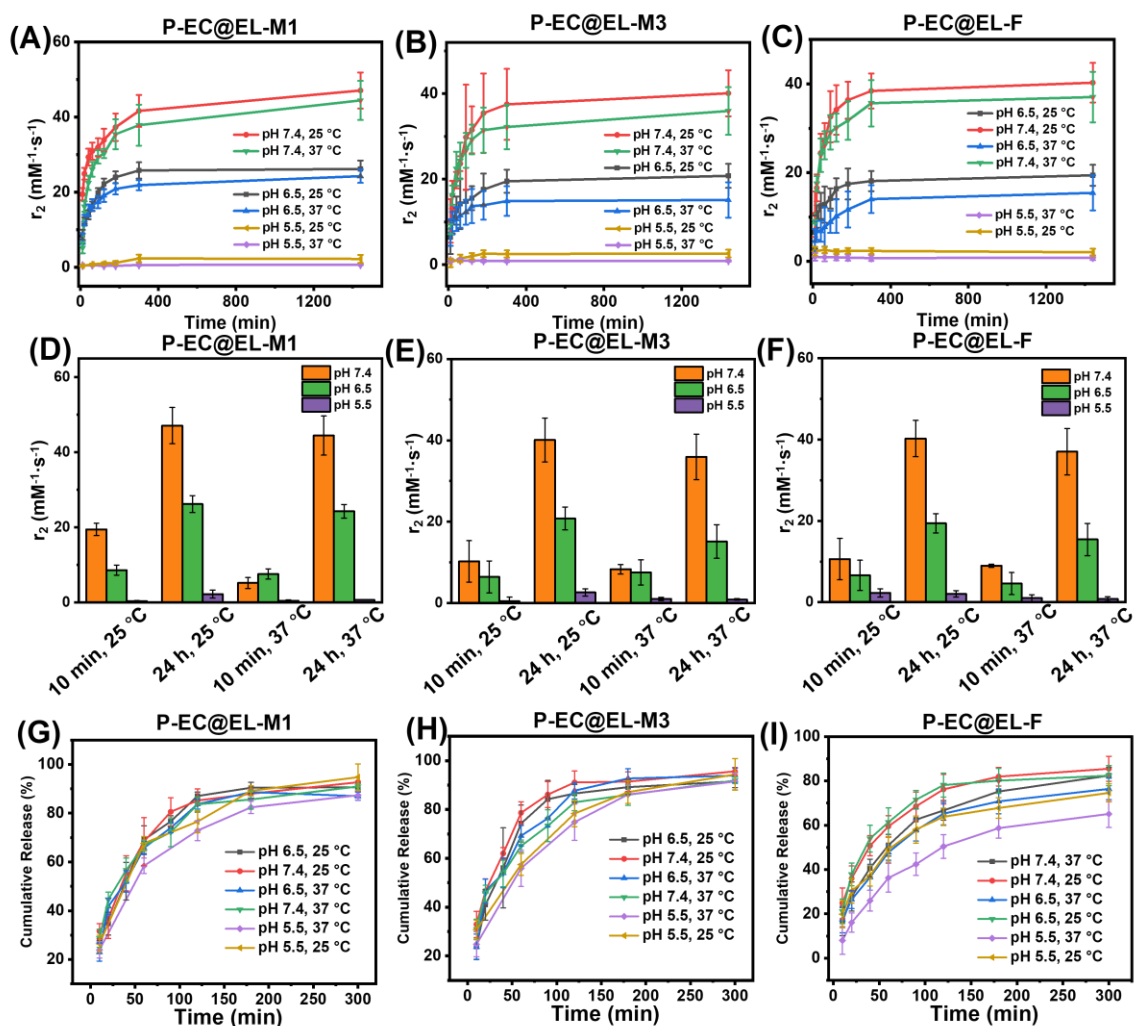
Fig. 4. Plots showing the change in transverse relaxation (r_2) of (A) P-EC@EL-M1; (B) P-EC@EL-M3; and, (C) P-EC@EL-F and the transverse relaxation (r_2) under different conditions (as labelled) of (D) P-EC@EL-M1; (E) P-EC@EL-M3; and (F) P-EC@EL-F. Also displayed are plots showing carmofur release (by UV-vis spectroscopy) from (G) P-EC@EL-M1; (H) P-EC@EL-M3; and, (I) P-EC@EL-F.

In order to directly compare with the relaxivity data, carmofur release was repeated in PBS at pH 7.4 or 6.5 with 0.1% xanthan gum and quantified by UV-vis spectroscopy alongside relaxivity changes (Fig. 4G-I). 0.1 % w/v xanthan gum were used to prevent the aggregation of microparticles and provide homogenous suspension for relaxivity measurement, which has little influence on r_2 values. The presence of xanthan gum causes the release milieu to have a gel-like consistency, which makes it impossible to transfer between different pH media; thus, experiments were performed only at pH 6.5 or 7.4, with no initial acid stage. All the systems displayed rapid release of carmofur over 3 hours, consistent with the *in vitro* drug release tests performed without xanthan (Fig. 3). When the pH is above 5.5, the r_2 value also consistently increased over 3 hours (Fig. 4A-C). To explore the relationship between carmofur release and relaxivity at these pHs, plots of cumulative carmofur release *vs* r_2 were constructed. These reveal a clear linear correlation between the two parameters, with R^2 ranging from 0.92 to 0.99 except for P-EC@EL-F at pH 6.5 and 37 °C, whose R^2 was slightly lower at 0.86 (Fig. S11). This indicates that changes in r_2 signal directly correspond to carmofur release, meaning that MRI

could be exploited as a non-invasive means of monitoring *in situ* drug release in environments such as the small intestine and colon. This approach could provide a non-invasive route to quantification of drug release at a site of interest, and could prove particularly helpful in treatments using highly toxic chemotherapy.

To validate the predictive ability of the r_2 data, equations correlating carmofur release (%) with relaxation behaviour of P-EC@EL-F (Table 2 and Fig. S12) were established as examples to predict carmofur release in a new series of experiments. In these, relaxation behaviour changes were determined for P-EC@EL-F (n=3) and used to predict the extent of carmofur release. The latter was then quantified by UV-vis spectroscopy and compared with r_2 predictions. The r_{2_max} is the maximum relaxivity value possible with the formulation, which manifests in our experiments as the relaxivity after 24 h, r_{2_24}. In the predictive equations we use r_{2_t}/r_{2_24} instead of r_2 because the MRI signal intensity is related both to the relaxivity properties of the CA and also to its local concentration. In the clinic, the local CA concentration might differ as a result of varied dosages, body volumes or other pathological conditions. Hence, the r_2 values in each system were normalised by calculating r_{2_t}/r_{2_max}. Plots comparing the predicted and observed release profiles are presented in Fig. 5.

Table 2.

Mathematical relationships between cumulative drug release (DR) and relaxation profiles (r_{2_t}/r_{2_24}) for P-EC@EL-F.

Temperature(°C)	pH	Fitting equation	R^2
25	7.4	$DR\ (\%) = 89.4\dfrac{r_{2\_t}}{r_{2\_24}} - 0.74$	0.9904
37	7.4	$DR\ (\%) = 80.3\dfrac{r_{2\_t}}{r_{2\_24}} - 3.1$	0.9683
25	6.5	$DR\ (\%) = 116.6\dfrac{r_{2\_t}}{r_{2\_24}} - 19.3$	0.9526
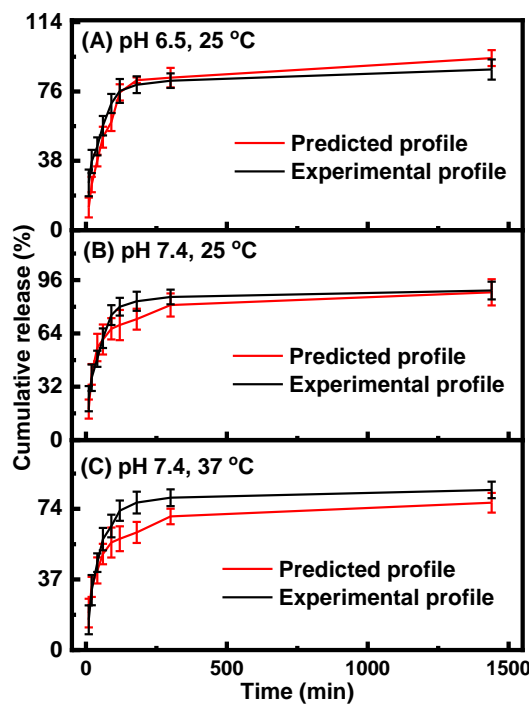
Fig. 5. Plots of experimental (black) and predicted (red) carmofur release from P-EC@EL-F at (A) pH 6.5, 25 °C; (B) pH 7.4, 25 °C (B); and (C) pH 7.4, 37 °C. Experiments were performed in PBS buffers at 2 mg/mL.

From Fig. 5 it is clear that the predicted drug release curves based on r_2 are very similar to the data obtained by UV-vis spectroscopy, indicating the potency of our theranostic approach. Two fit factors F_1 (the difference factor) and F_2 (the similarity factor) (Equations 2 and 3, respectively) were applied to statistically compare the experimental dissolution profile acquired by UV-vis and that calculated based on relaxivity (Moore and Flanner, 1996).

$$F_1 = \left(\frac{\sum|R_t - T_t|}{\sum R_t}\right) \times 100 \qquad \textbf{(2)}$$

$$F_2 = 50 \times \log\left\{100 \times \left[1 + \frac{\sum(R_t - T_t)^2}{n}\right]^{-0.5}\right\} \qquad \textbf{(3)}$$

502 R_t and T_t represents the percentage of active pharmaceutical ingredient released from reference and
503 test samples at time point t, respectively, and n is the number of time points. Two dissolution profiles
504 are regarded to be "same" or "equivalent" when F_1 is less than 15 and F_2 is greater than 50 (Freitag,
505 2001). Here we use the experimental release data obtained by UV-vis spectroscopy as the reference
506 (R_t), and the predicted data as the test (T_t). The results are shown in Table 3. The F_1 and F_2 values of
507 P-EC@EL-F all lie in the range of "equivalent", suggesting the reliability of our predicted curves.

508

509 **Table 3. F_1 (difference factor) and F_2 (similarity factor) values comparing the predicted vs**
510 **experimental release plots of P-EC@EL-F.**

Sample	F_1	F_2
pH 6.5, 25 ℃	10.6	54.4
pH 7.4, 25 ℃	9.2	58.1
pH 7.4, 37 ℃	14.1	51.2

511

512 This work presents a proof-of-concept study looking to prepare dual responsive theranostic systems
513 by EHDA, and exploring the effect of formulation morphology on performance. Overall, it is clear that
514 the core@shell fibre formulation developed has pH- and temperature-responsive drug release and
515 MRI properties, while the microparticles do not. The fibres are able to prevent SPION and carmofur
516 release in the low-pH environments of the stomach. Drug release profiles can be accurately predicted
517 using relaxivity values. The increase in drug release rate and relaxivity at lower temperatures could be
518 exploited to accelerate carmofur release via a hypothermia treatment. It should be noted that both
519 carmofur and SPION release is generally higher at the physiological pH than at the slightly acidic pH
520 typical of the tumour. The increased release of SPIONs at pH 7.4 is not problematic, because SPIONs
521 are negative contrast agents that make MR images darker. Hence, the higher r_2 values observed at
522 neutral pH values will lead to healthy tissue having darker contrast in the images, and cancerous sites
523 at lower pHs can be distinguished by dint of their appearing brighter. However, more work is required
524 to develop the formulations further and effectively exploit the small differences between physiological
525 and tumour microenvironment pH to target drug release to a tumour. That said, the differences in
526 release at pH 5.5 and 7.5 are small and the fibre formulation is effective at preventing release in the
527 acidic pH of the stomach, and thus targeting to the small intestine and colon is possible using the P-
528 EC@EL-F system.

529

530 **Conclusions**

531 In this study, two core@shell microparticles and a core@shell fibre were fabricated via
532 electrohydrodynamic methods and fully characterized. All the formulations have pH responsive
533 polymer shells loaded with SPIONs, and a thermo-responsive core with an amorphous dispersion of a
534 model chemotherapeutic drug, carmofur. Electron microscopy images showed that microparticle
535 shape changes with the w/w ratio of core to shell polymer, from a concave shape with a low core

polymer mass content to a spherical shape with greater weight percentage of core polymer. The fibres generally have regular core@shell morphology. The encapsulation of SPIONs in the shell polymer can prevent them from digestion in acidic conditions such as gastric fluids. *In vitro* drug release studies reveal that the core@shell fibres displayed a thermo-responsive release profile, and can work as potent delayed-release oral treatments for colon cancer. In contrast, the microparticles do not show notable stimuli-responsiveness. This difference is attributed to the different surface area to volume ratios of the two types of formulation. The MRI contrast agent behavior (relaxivity) was monitored and showed a pH responsive profile between pH 5.5 to 7.4. The relaxivity of suspensions of the formulations could be used to predict the extent of drug release. The systems developed in this work thus have the potential to allow non-invasive monitoring of drug release *in vivo* via changes in MRI signal intensity.

Declaration of Competing Interest

The authors declare that there is no conflict of interest.

References

Angelakeris, 2017 M. Angelakeris

Magnetic nanoparticles: A multifunctional vehicle for modern theranostics

Biochim. Biophys. Acta. Gen. Subj., 1861(6) (2017), pp. 1642-1651

Chang et al., 2011 B. Chang, X. Sha, J. Guo, Y. Jiao, C. Wang, W. Yang

Thermo and pH dual responsive, polymer shell coated, magnetic mesoporous silica nanoparticles for controlled drug release

J. Mater. Chem., 21(25) (2011), pp. 9239-9247

Davies et al., 2013 G.L. Davies, I. Kramberger, J. J. Davis

Environmentally responsive MRI contrast agents

Chem. Comm., 49(84) (2013), pp. 9704-9721

Evans et al., 1988 D.F. Evans, G. Pye, R. Bramley, A. Clark, T.J. Dyson, J.D. Hardcastle

Measurement of gastrointestinal pH profiles in normal ambulant human subjects

Gut, 29(8) (1988), pp. 1035-1041.

570   Freitag, 2001 G. Freitag

571   **Guidelines on dissolution profile comparison**

572   Drug Information J., 35(3) (2001), pp. 865-874

573   Haacke and Reichenbach, 2014 E.M. Haacke, J.R. Reichenbach

574   **Susceptibility weighted imaging in MRI: basic concepts and clinical applications**

575   John Wiley & Sons., (2014)

576   Hei et al., 2017 M. Hei, J. Wang, K. Wang, W. Zhu, P.X. Ma

577   **Dually responsive mesoporous silica nanoparticles regulated by upper critical solution**
578   **temperature polymers for intracellular drug delivery**

579   J. Mater. Chem. B, 5(48) (2017), pp. 9497-9501.

580   Hudecki et al., 2017 A. Hudecki, J. Gola, S. Ghavami, M. Skonieczna, J. Markowski, W. Likus, M.
581   Lewandowska, W. Maziarz, M.J. Los

582   **Structure and properties of slow-resorbing nanofibers obtained by (co-axial)**
583   **electrospinning as tissue scaffolds in regenerative medicine**

584   PeerJ, 5 (2017), pp. e4125.

585   Jha et al., 2020 A. Jha, M.K. Viswanadh, A.S. Burande, A.K. Mehata, S. Poddar, K. Yadav, S.K. Mahto,
586   A.S. Parmar, M.S. Muthu

587   **DNA biodots based targeted theranostic nanomedicine for the imaging and treatment of**
588   **non-small cell lung cancer**

589   Int. J. Biol. Macromol., 150 (2020), pp. 413-425

590   Jin et al., 2016 M. Jin, D.G. Yu, C.F.G.C. Geraldes, G.R. Williams, S.W.A. Bligh

591   **Theranostic Fibers for Simultaneous Imaging and Drug Delivery**

592   Mol. Pharm., 13(7) (2016), pp. 2457-2465

593   Jin et al., 2016 M. Jin, D. G. Yu, X. Wang, C.F.G.C. Geraldes, G.R. Williams, S.W.A. Bligh

594   **Electrospun Contrast‐Agent‐Loaded Fibers for Colon‐Targeted MRI**

595   Adv. Healthc. Mater., 5(8) (2016), pp. 977-985

596   Jin et al., 2014 R. Jin, B. Lin, D. Li, H. Ai

597   **Superparamagnetic iron oxide nanoparticles for MR imaging and therapy: design**
598   **considerations and clinical applications**

599   Curr. Opin. Pharmacol. 18 (2014), pp. 18-27

600   Johnson et al., 2014 R.P. Johnson, J.V. John, I. Kim

Poly(l-histidine)-containing polymer bioconjugate hybrid materials as stimuli-responsive theranostic systems

J. Appl. Polym. Sci., 131(18) (2014)

Jordan et al., 1999 A. Jordan, R. Scholz, P. Wust, H. Fähling, R. Felix

Magnetic fluid hyperthermia (MFH): Cancer treatment with AC magnetic field induced excitation of biocompatible superparamagnetic nanoparticles

J. Magn. Magn. Mater., 201(1-3) (1999), pp. 413-419

Kang et. al, 2017 T. Kang, F. Li, S. Baik, W. Shao, D. Ling, T. Hyeon

Surface design of magnetic nanoparticles for stimuli-responsive cancer imaging and therapy

Biomaterials, 136 (2017), pp. 98-114

Komur et al., 2017 B. Komur, F. Bayrak, N. Ekren, M.S. Eroglu, F.N. Oktar, Z.A. Sinirlioglu, S. Yucel, O. Guler, O. Gunduz

Starch/PCL composite nanofibers by co-axial electrospinning technique for biomedical applications

Biomed. Eng. Online, 16(1) (2017), pp. 1-13

Laurent et al., 2011 S. Laurent, S. Dutz, U.O. Häfeli, M. Mahmoudi

Magnetic fluid hyperthermia: focus on superparamagnetic iron oxide nanoparticles

Adv. Colloid Interface Sci., 166(1-2) (2011), pp. 8-23

Lin et al., 2017 J.T. Lin, J.K. Du, Y.Q. Yang, L.Li, D.W. Zhang, C.L. Liang, J. Wang, J. Mei, G.H. Wang

pH and redox dual stimulate-responsive nanocarriers based on hyaluronic acid coated mesoporous silica for targeted drug delivery

Mater. Sci. Eng. C, 81 (2017), pp. 478-484

Liu et al., 2017 M. Liu, X. Song, Y. Wen, J.L. Zhu, J. Li

Injectable thermoresponsive hydrogel formed by alginate-g-Poly(N-isopropylacrylamide) that releases doxorubicin-encapsulated micelles as a smart drug delivery system

ACS Appl. Mater. Interfaces, 9(41) (2017), pp. 35673-35682

Mahmoudi et al., 2011 M. Mahmoudi, S. Sant, B. Wang, S. Laurent, T. Sen

Superparamagnetic iron oxide nanoparticles (SPIONs): development, surface modification and applications in chemotherapy

Adv. Drug Deliv. Rev., 63(1-2) (2011), pp. 24-46

Mano, 2008 J.F. Mano

Stimuli‑responsive polymeric systems for biomedical applications

Adv. Eng. Mater. 10(6) (2008), pp. 515-527

Moore and Flanner, 1996 J.W. Moore, H.H. Flanner

Mathematical comparison of dissolution profiles

Pharm. Technol., 20(6) (1996), pp. 64-74

Neuwelt et al., 2015 A. Neuwelt, N. Sidhu, C.A. Hu, G. Mlady, S.C. Eberhardt, L.O. Sillerud

Iron-based superparamagnetic nanoparticle contrast agents for MRI of infection and inflammation

AJR Am J Roentgenol 204(3) (2015), pp. W302-W313

Parsi et al., 2017 M.A. Parsi, A.J. Trindade, M.S. Bhutani, J. Melson, U. Navaneethan, N. Thosani, G. Trikudanathan, R.R. Watson, J.T. Maple

Cryotherapy in gastrointestinal endoscopy

VideoGIE, 2(5) (2017), pp. 89-95

Patil et al., 2020 B.R. Patil, S.Y. Kang, D.H. Jung, P.G. Avaji, Y.J. Jun, H.J. Lee, Y.S. Sohn

Design of a Novel Theranostic Nanomedicine (III): Synthesis and Physicochemical Properties of Tumor-Targeting Cisplatin Conjugated to a Hydrophilic Polyphosphazene

Int. J. Nanomed., 15 (2020), pp. 981-990

Perera et al., 2018 A.S. Perera, S. Zhang, S. Homer-Vanniasinkam, M.O. Coppens, M.

Polymer–magnetic composite fibers for remote-controlled drug release

ACS Appl. Mater. Interfaces, 10(18) (2018), pp. 15524-15531

Primrose, 2002 J. Primrose

Treatment of colorectal metastases: surgery, cryotherapy, or radiofrequency ablation

Gut, 50(1) (2002), pp. 1-5

Rose et al., 2016 L.C. Rose, J.C. Bear, P. Southern, P.D. McNaughter, R.B. Piggott, I.P. Parkin, S. Qi, B.P. Hills, A. G. Mayes

On-demand, magnetic hyperthermia-triggered drug delivery: optimisation for the GI tract

J. Mater. Chem. B, 4(9) (2016), pp. 1704-1711

Sanchez-Vazquez et al., 2017 B. Sanchez-Vazquez, A.J. Amaral, D.G. Yu, G. Pasparakis, G.R. Williams

Electrosprayed Janus particles for combined photo-chemotherapy

AAPS PharmSciTech 18(5) (2017), pp. 1460-1468

Sokolov et al., 2017 I. L. Sokolov, V.R. Cherkasov, A.A. Tregubov, S.R. Buiucli, M.P. Nikitin

664 **Smart materials on the way to theranostic nanorobots: Molecular machines and**
665 **nanomotors, advanced biosensors, and intelligent vehicles for drug delivery**

666 Biochim. Biophys. Acta Gen. Subj., 1861(6) (2017), pp. 1530-1544

667 Wen et al., 2018 P. Wen, T.G. Hu, L. Li, M.H. Zong, H. Wu

668 **A colon-specific delivery system for quercetin with enhanced cancer prevention based on**
669 **co-axial electrospinning**

670 Food Funct., 9(11) (2018), pp. 5999-6009

671 Williams et. al, 2018 G.R. Williams, B.T. Raimi-Abraham, C. Luo

672 **Nanofibres in Drug Delivery**

673 UCL Press, 2018

674 Xu et al., 2013 S. Xu, Q. Xu, J. Zhou, J. Wang, N. Zhang, L. Zhang

675 **Preparation and characterization of folate-chitosan-gemcitabine core–shell nanoparticles**
676 **for potential tumor-targeted drug delivery**

677 J. Nanosci. Nanotechnol., 13(1) (2018), pp. 129-138

678 Zhang et al., 2014 L. Zhang, L. Wang, B.L. Guo, P.X. Ma

679 **Cytocompatible injectable carboxymethyl chitosan/N-isopropylacrylamide hydrogels for**
680 **localized drug delivery**

681 Carbohydr. Polym., 103 (2014), pp. 110-118

682 Zhang et al., 2020 Z. Zhang, C.J. Wells, A.M. King, J.C. Bear, G.L. Davies, G.R. Williams

683 **pH-Responsive nanocomposite fibres allowing MRI monitoring of drug release**

684 J. Mater. Chem. B, 8(32) (2020), pp. 7264-7274

685 Zhao et al., 2015 P. Zhao, M. Zheng, Z. Luo, P. Gong, G. Gao, Z. Sheng, C. Zheng, Y. Ma, L. Cai

686 **NIR-driven Smart Theranostic Nanomedicine for On-demand Drug Release and Synergistic**
687 **Antitumour Therapy**

688 Sci. Rep. 5(1) (2015), pp. 1-14

689

690